Integrated silicon carbide modulator for CMOS photonics

Keith Powell[1,2], Liwei Li[1], Amirhassan Shams-Ansari[2], Jianfu Wang[1], Debin Meng[1], Neil Sinclair[2,3], Jiangdong Deng[4], Marko Lončar[2*] & Xiaoke Yi[1*]

Author affiliations. [1]School of Electrical and Information Engineering, the University of Sydney, NSW 2006, Australia. [2]John A. Paulson School of Engineering and Applied Sciences, Harvard University, Cambridge, MA 02138, USA. [3]Division of Physics, Mathematics and Astronomy, and Alliance for Quantum Technologies (AQT), California Institute of Technology, 1200 E. California Boulevard, Pasadena, CA 91125, USA. [4]Center for Nanoscale Systems, Harvard University, Cambridge, MA 02138, USA.
*E-mail: loncar@seas.harvard.edu; xiaoke.yi@sydney.edu.au

The electro-optic modulator encodes electrical signals onto an optical carrier, and is essential for the operation of global communication systems and data centers that society demands[1]. An ideal modulator results from scalable semiconductor fabrication and is integratable with electronics. Accordingly, it is compatible with complimentary metal-oxide semiconductor (CMOS) fabrication processes. Moreover, modulators using the Pockels effect enables low loss, ultrafast and wide-bandwidth data transmission. Although strained silicon-based modulators could satisfy these criteria, fundamental limitations such as two-photon absorption, poor thermal stability and a narrow transparency window hinder their performance. On the other hand, as a wide bandgap semiconductor matrial, silicon carbide is CMOS compatible and does not suffer from these limitations. Due to its combination of color centers, high breakdown voltage, and strong thermal conductivity, silicon carbide is a promising material for CMOS electronics and photonics with applications ranging from sensors to quantum and nonlinear photonics[2-4]. Importantly, silicon carbide exhibits the Pockels effect, but a modulator has not been realized since the discovery of this effect more than three decades ago. Here we design, fabricate, and demonstrate the first Pockels modulator in silicon carbide. Specifically, we realize a waveguide-integrated, small form-factor, gigahertz-bandwidth modulator that can operate using CMOS-level drive voltages on a thin film of silicon carbide on insulator. Furthermore, the device features no signal degredation and stable operation at high optical intensities (913 kW/mm^2), allowing for high optical signal-to-noise ratios

for long distance communications. Our work unites Pockels electro-optics with a CMOS platform to pave the way for foundry-compatible integrated photonics.

The convergence of photonics and CMOS electronics empowers photonic integrated circuits to meet the ever-increasing demand for data throughput in information systems[5,6]. In particular, the electro-optic (EO) modulator is at the center of this convergence as a critical component for encoding electrical signals onto light for applications in datacenters, telecommunication networks and microwave photonic systems. State-of-the-art modulators based on silicon, the workhorse material of electronics, rely on the free carrier plasma dispersion effect. This effect is intrinsically absorptive and nonlinear as it causes coupled phase and amplitude modulation, which distorts the signal modulation amplitude and restrict usage of advanced modulation formats[7]. Alternatively, EO modulators based on the Pockels effect i.e. linear EO effect, which exists in non-centrosymmetric crystals, allows the refractive index to vary linearly and rapidly in proportion to an applied electric field. Consequently, Pockels modulators are exploited to achieve high data rates and conversion efficiencies without the addition of optical loss[8]. The Pockels effect is not present in most materials in the CMOS family, including silicon and silicon nitride. Aluminum nitride (AlN) exhibits the Pockels effect with non-equal EO tensors, and has relatively low refractive index, which increases the complexity in dense optoelectronic integration[9]. Modifications to the crystal symmetry of CMOS materials by strain have been proposed to realize EO modulators[10-12], but suffer from trade-offs fabrication complexity. For example, strained silicon[11,12] suffers from two-photon optical absorption and poor thermal stability that is inherent to silicon. Furthermore, the relatively small indirect bandgap of silicon prevents the usage of silicon waveguide in the visible spectrum range, which is of great interest for applications in sensing and quantum optics[13,14]. Commonly-used lithium niobate ($LiNbO_3$) Pockels modulators have a strong EO coefficient[15]. However, they suffer from signal-distortion induced by photorefraction that worsens with increasing optical powers[16], and is avoided by post-modulation amplification in applications. Moreover, low costs and high yields on chip are required, as permitted by the integration via CMOS compatible fabrication[17].

One CMOS-compatible material that exhibits the Pockels effect is silicon carbide (SiC)[18]. In particular, the cubic (3C) polytype of SiC has the largest measured EO coefficient (~ 2.7 pm/V at 633 nm) of all SiC polytypes and has equal elements of the EO tensor[19], which simplifies optoelectronic integration. Moreover, the wide bandgap of SiC allows broadband optical transparency from ultraviolet to infrared. Despite this, a SiC-based Pockels modulator has not been experimentally demonstrated due to poor crystal quality and difficulty obtaining low-loss waveguides[20–23]. Although 3C-SiC can be grown directly onto a silicon substrate, it has been difficult to realize high-quality thin films, due to crystal defects associated with this approach[23,24]. Wafer bonding techniques[25] and annealing processes[26] have been explored to address these problems. Yet, the former demonstrates multimode waveguides while the latter still results in a high (7 dB/cm) optical loss. These issues undermine a 3C-SiC Pockels modulator, specifically one that features single-mode waveguides for stable and high extinction-ratio ring modulators or quantum applications[27].

Moreover, due to its high electron mobility, as well as robust properties[27-30], SiC is a compelling semiconductor material for next-generation CMOS electronics and a contender for realizing monolithic integration of quantum and nonlinear photonics[2,3,27,31,32]. By taking the advantage of its high thermal conductivity[33], wide band-gap, low thermo-optic coefficient[26] and high refractive index (~2.57)[34], SiC offers the possibility of densely integrated and robust photonic devices with low fabrication costs via CMOS-compatible nanofabrication[35] and the potential for integration with electronics.

Here we present the first SiC EO modulator. Optical modulation is achieved by electrically driving a microring resonator in sub-micron-wide 3C-SiC on insulator waveguides via the Pockels effect. A microring is chosen to enable a compact device footprint (90 μm^2), while maintaining high modulation performance at low voltage. The modulator is fabricated with a CMOS-compatible process and operates at a transmission rate of up to 15 gigabits per second using CMOS-level drive voltages. Importantly, we reduce the impact of polycrystal grains and waveguide surface roughness to demonstrate ~5.4 dB/cm optical loss using a single-mode waveguide. As a result of our work, we measure the Pockels coefficient

(1.5 pm/V) of 3C-SiC at an infrared wavelength for the first time. Moreover, the modulator is able to operate continuously with high optical intensities of up to 913 kW/mm^2 without signal degradation, facilitating low-noise microwave photonics[36] or parametric conversion of single photons[37].

The fabrication of the integrated 3C-SiC modulator begins with the 530 nm-thick SiC layer with a low crystal defect density (see Methods) to reduce the scattering or absorption losses and increase EO interaction. Figure 1a shows an optical micrograph of a fabricated modulator capable of operating using a CMOS digital to analog converter (DAC). The modulator consists of a pair of 3C-SiC vertical grating couplers (VGCs) as optical input and output ports, an optical waveguide ring resonator with a loaded quality (Q_L) factor of 34,310 to balance modulation efficiency and bandwidth[38], and microwave strip line electrodes to deliver electrical signals. The waveguides and the VGCs are structured by electron beam lithography (EBL) (see Methods), in which a typical waveguide width of 800 nm is chosen to maintain single mode operation with high optical mode confinement. The electrodes consist of a pair of ground electrodes placed next to the sides of the waveguide and a signal electrode above the waveguide (Fig.1b). A 1-μm-thick top cladding SiO2 layer is deposited to separate the electrode to the waveguide, which prevents optical loss from mode interaction with the metal. Figure 1c shows a cross sectional scanning electron micrograph (SEM) of the modulator to illustrate the geometries of the waveguide and electrodes. The electrode thickness (~500 nm) is chosen to reduce radio frequency (RF) loss due to the skin effect. As depicted in Fig. 1d, when a voltage is applied across the signal and ground electrodes, a vertical electric field is induced predominantly in the vertical direction overlapping with the optical mode to probe the Pockels effect. The ring cavity enables the phase change to be translated into an intensity modulated output, where the resonant enhancement of the modulator allows for a small device footprint and low drive voltage operation. Figure 1e shows a SEM of our etched waveguide, which can achieve a root-mean-squared sidewall roughness less than 2.4 nm[26] facilitating absorption limited optical loss. To qualify the optical loss, the optical spectrum of the microring resonator with critically coupled resonances operating at the telecommunication wavelengths (1569 nm - 1600 nm) is measured to reveal single mode

operation (Fig. 1f) with a resonance linewidth of 36.9 pm (Fig. 1g). The obtained intrinsic Q (Q_I) is 86,000 corresponding to a linear propagation loss of ~5.4 dB/cm.

To characterize the maximum operational bandwidth of our fabricated modulator, we examine the EO response at an optical input power of 6.8 mW (see Methods), which shows a 3 dB bandwidth of 7.1 GHz (Fig. 2a). The bandwidth is limited by the cavity photon lifetime of 28 ps, calculated based on the measured cavity linewidth (45 pm), that corresponds to the modulation bandwidth of around 5.7 GHz. The electrode circuit of the modulator has much broader spectral response exceeding 30 GHz, as indicated in the inset of Fig. 2a. Therefore, higher bandwidths could be achieved via reducing the cavity Q factor, however this will result in a lower modulation index with the same RF signal strength[38].

To determine the EO performance of the modulator, we use light of 1544.1 nm wavelength and drive the modulator with frequencies between 2.5 GHz and 17.5 GHz with a peak to peak drive voltage (Vpp) of 1V (see Methods). The generation of double sidebands seen in the optical spectrum explicitly demonstrates the resultant intensity modulation (Fig. 2b). For increasing frequency, a reduction in sideband power is observed, consistent with the roll off induced by the resonant linewidth. For the modulation frequency less than the resonator linewidth e.g. 2.5 GHz, the modulator can achieve an extinction ratio of 3dB with Vpp = 8V. Using the measured optical spectrum and determining the electric field strength inside the waveguide, we are able to extract the Pockels coefficient as 1.5 pm/V (see Methods) which is higher than AlN (1pm/V)[9] . The combination with a low permittivity (~9.7)[39] and high refractive index[34] also allows for more efficient utilization of the linear EO effect in 3C-SiC over other materials, e.g. LiNbO3. With direct current (DC) voltages, a resonance shift of 0.11 pm/V (see Methods) is measured which is lower than the measured RF shift likely due to shielding caused by trapped charges in the silicon rich SiO_x layer. This could be avoided by annealing or using higher purity thermal oxide.

To quantify the performance of our modulator for data transmission, we demonstrate low voltage operation with digital modulation (see Methods). Using a non-return-to-zero (NRZ) pseudo random bit sequence (PRBS) of 2^7 bits, we drive the modulator directly from a CMOS DAC operating with a Vpp

ranging from 0.2 V to 2 V (Fig. 3a). Figure 3b shows the measured binary data over a period of 5 ns at a data rate of 5 Gb/s, with an optical input power of 6.8mW using drive voltages of 2 Vpp and 1.2 Vpp, showing that the modulator correctly modulates the light intensity according to the applied digital sequence. Figure 3c shows the modulator operates at low drive voltages and an optical input power of 6.8 mW across a range of modulation speeds, with the eye-diagram quality (Q_E) factors greater than 2.7, which lead to bit-error ratios (BERs) below the hard-decision forward error correction (HD-FEC) limit (3.8×10^{-3})[40,41]. While the drive voltage is reduced from Vpp=2V to 1.2V, the modulator still maintains an open 5Gb/s NRZ eye diagram, allowing for successful data transmission and detection. With Vpp = 2 V and an optical input power of 6.8 mW, the modulator supports bit rates up to 10 Gb/s, limited by the cavity photon lifetime bandwidth (5.7 GHz).

The ability for modulator to handle high optical powers is important for enhancing signal to noise ratio in the growing field of microwave photonic applications[4,36], as well as for quantum transduction[37] and nonlinear photonics[27]. To quantify the operation at high and continuous optical intensities, we measure the EO responses of the modulator with varied optical input power. The results are shown in Fig. 4a, in which the optical intensity within the waveguide at the resonance wavelength is calculated from the peak circulating power within the ring resonator[42]. It shows by increasing the optical intensity from 254 kW/mm^2 to 913 kW/mm^2, the EO response is enhanced by 10.2 dB without evidence of signal distortion. The observed eye diagrams (Fig. 4b) also exhibit enlarged openings at 15 Gb/s with increased optical intensities, which shows improved modulation performance for digital signals and the ability to reach larger bandwidths. Moreover, Fig. 4c shows at an optical intensity of 913 kW/mm^2, the Q_E factors extracted from the measured eye diagrams for all data rates at Vpp = 2 V are over 2.7, confirming the operation of the modulator at high optical intensities.

To distinguish SiC for optical and electrical integration, we compare the material parameters of several EO modulator platform (Fig. 4d). The large thermal conductivity of 3C-SiC (490 W/(m·K)) that is almost double that of AlN and more than 12 fold larger than $LiNbO_3$, together with the high Moh's hardness and

large Young's modulus, make the modulator unrivaled for high power EO applications and co-integration with CMOS electronics. Furthermore, the ultra-high breakdown field of 3C-SiC (4 MV/cm) which is 18 fold higher than $LiNbO_3$ enables the possibility to integrate RF amplifiers on chip with the modulator, and makes it resistant to electro-magnetic attacks from RF bursts. Moreover, the high radiation hardness of SiC also presents advantages in harsh operating environments[29].

We demonstrate an integrated Pockels modulator in SiC with a drive voltage compatible with CMOS electronics, a small device footprint, and continuous low-noise data modulation at high optical intensities. The SiC EO modulator opens new opportunities for direct optoelectronic integration using CMOS foundries with the benefit to various applications ranging from optical networks, chip scale interconnects, RF and microwave photonics and quantum information. Our work constitutes an essential piece in the vision of a thin film SiC platform consisting of monolithic integration of modulators, photodiodes, quantum defects and protocols to realize on chip photonics. Finally, the ability to integrate with CMOS electronics could inspire a new generation of integrated optoelectronic devices for photonic signal processing, chip-chip or intra-chip interconnects ushering in a new era of optical based electronics.

REFERENCES

1. Reed, G. T., Mashanovich, G., Gardes, F. Y. & Thomson, D. J. Silicon optical modulators. *Nat. Photonics* **4**, 518–526 (2010).
2. Lukin, D. M. *et al.* 4H-silicon-carbide-on-insulator for integrated quantum and nonlinear photonics. *Nat. Photonics* **14**, 330–334 (2020).
3. Anderson, C. P. *et al.* Electrical and optical control of single spins integrated in scalable semiconductor devices. *Science* **366**, 1225–1230 (2019).
4. Ghelfi, P. *et al.* A fully photonics-based coherent radar system. *Nature* **507**, 341–345 (2014).
5. Xu, Q., Schmidt, B., Pradhan, S. & Lipson, M. Micrometre-scale silicon electro-optic modulator. *Nature* **435**, 325–327 (2005).

6. Towards systems-on-a-chip. *Nat. Photonics* **12**, 311 (2018).

7. Reed, G. T. *et al.* Recent breakthroughs in carrier depletion based silicon optical modulators. *Nanophotonics* **3**, 229–245 (2014).

8. Boyd, R. W. *Nonlinear Optics*. (Academic, Cambridge, 2003).

9. Xiong, C., Pernice, W. H. P. & Tang, H. X. Low-loss, silicon integrated, aluminum nitride photonic circuits and their use for electro-optic signal processing. *Nano Lett.* **12**, 3562–3568 (2012).

10. Alexander, K. *et al.* Nanophotonic Pockels modulators on a silicon nitride platform. *Nat. Commun.* **9**, 1–6 (2018).

11. Jacobsen, R. S. *et al.* Strained silicon as a new electro-optic material. *Nature* **441**, 199–202 (2006).

12. Berciano, M. *et al.* Fast linear electro-optic effect in a centrosymmetric semiconductor. *Commun. Phys.* **1**, 1–9 (2018).

13. Awschalom, D.D., Hanson, R., Wrachtrup, J. *et al.* Quantum technologies with optically interfaced solid-state spins. *Nat. Photonics* **12**, 516–527 (2018).

14. Aharonovich, I., Englund, D. & Toth, M. Solid-state single-photon emitters. *Nat. Photonics* **10**, 631–641 (2016).

15. Wang, C. *et al.* Integrated lithium niobate electro-optic modulators operating at CMOS-compatible voltages. *Nature* **562**, 101–104 (2018).

16. Jiang, H. *et al.* Fast response of photorefraction in lithium niobate microresonators. *Opt. Lett.* **42**, 3267–3270 (2017).

17. Safian, R., Teng, M., Zhuang, L. & Chakravarty, S. Foundry-compatible thin film lithium niobate modulator with RF electrodes buried inside the silicon oxide layer of the SOI wafer. *Opt. Express* **28**, 25843–25857 (2020).

18. Tang, X., Irvine, K. G., Zhang, D. & Spencer, M. G. Linear electro-optic effect in cubic silicon

carbide. *Appl. Phys. Lett.* **59**, 1938–1939 (1991).

19. Barrios, C. A., Thomas, C. I., Spencer, M. & Lipson, M. 3C-SiC modulator for high-speed integrated photonics. *Materials Research Society Symposium - Proceedings* **799**, 158–162 (2003).

20. Vonsovici, A., Reed, G. T. & Evans, A. G. R. β-SiC-on insulator waveguide structures for modulators and sensor systems. *Mater. Sci. Semicond. Process.* **3**, 367–374 (2000).

21. Liu, Y. M. & Prucnal, P. R. Low-loss silicon carbide optical waveguides for silicon-based optoelectronic devices. *IEEE Photonics Technol. Lett.* **5**, 704–707 (1993).

22. Reed, G. T. *et al.* Fabrication and evaluation of SiC optical modulators. *Silicon-based Hybrid Optoelectron. IV* **4654**, 145–156 (2002).

23. Cardenas, J. *et al.* High Q SiC microresonators. *Opt. Express* **21**, 16882–16887 (2013).

24. Lu, X., Lee, J. Y., Feng, P. X.-L. & Lin, Q. High Q silicon carbide microdisk resonator. *Appl. Phys. Lett.* **104**, 181103 (2014).

25. Fan, T., Moradinejad, H., Wu, X., Eftekhar, A. A. & Adibi, A. High-Q integrated photonic microresonators on 3C-SiC-on-insulator (SiCOI) platform. *Opt. Express* **26**, 25814–25826 (2018).

26. Powell, K. *et al.* High-Q suspended optical resonators in 3C silicon carbide obtained by thermal annealing. *Opt. Express* **28**, 4938–4949 (2020).

27. Lukin, D. M., Guidry, M. A. & Vučković, J. Integrated quantum photonics with silicon carbide: challenges and prospects. *PRX Quantum* **1**, 020102 (2020).

28. Atatüre, M., Englund, D., Vamivakas, N., Lee, S. Y. & Wrachtrup, J. Material platforms for spin-based photonic quantum technologies. *Nat. Rev. Mater.* **3**, 38–51 (2018).

29. Lee, T. H., Bhunia, S. & Mehregany, M. Electromechanical computing at 500°C with silicon carbide. *Science* **329**, 1316–1318 (2010).

30. Nakamura, D. *et al*. Ultrahigh-quality silicon carbide single crystals. *Nature* **430**, 1009–1012

(2004).

31 Gordon, L., Janotti, A. & Van de Walle, C.G. Defects as qubits in 3C- and 4H-SiC. *Physical Review B* **92**, 045208 (2015).

32. Whiteley, S. J. *et al*. Spin–phonon interactions in silicon carbide addressed by Gaussian acoustics. *Nat. Phys.* **15**, 490–495 (2019).

33. Yamaoka, S. *et al*. Directly modulated membrane lasers with 108 GHz bandwidth on a high-thermal-conductivity silicon carbide substrate. *Nat. Photonics* **15**, 28–35 (2021).

34. Tropf, W. J., Thomas, M. E. & Linevsky, M. J. Infrared refractive indices and thermo-optic coefficients for several materials. *Optical Diagnostic Methods for Inorganic Transmissive Materials* **3425**, 160–171 (1998).

35. Nabki, F., Dusatko, T. A., Vengallatore, S. & El-Gamal, M. N. Low-stress CMOS-compatible silicon carbide surface-micromachining technology-part I: Process development and characterization. *J. Microelectromechanical Syst.* **20**, 720–729 (2011).

36. Marpaung, D., Yao, J. & Capmany, J. Integrated microwave photonics. *Nat. Photonics* **13**, 80–90 (2019).

37. Holzgrafe, J. *et al*. Cavity electro-optics in thin-film lithium niobate for efficient microwave-to-optical transduction. *Optica* **7**, 1714–1720 (2020).

38. Yu, H. *et al*. Trade-off between optical modulation amplitude and modulation bandwidth of silicon micro-ring modulators. *Opt. Express* **22**, 15178–15189 (2014).

39. Patrick, L. & Choyke, W. J. Static dielectric constant of SiC. *Physical Review B* **2**, 2255–2256 (1970).

40. Cho, J., Xie, C. & Winzer, P.J. Analysis of soft-decision FEC on non-AWGN channels. *Opt. Express* **20**, 7915–7928 (2012).

41. Asif, R. Advanced and flexible multi-carrier receiver architecture for high-count multi-core fiber based space division multiplexed applications. *Sci. Rep.* **6**, 27465 (2016).

42. Ikeda, K., Saperstein, R. E., Alic, N. & Fainman, Y. Thermal and Kerr nonlinear properties of plasma-deposited silicon nitride/ silicon dioxide waveguides. *Opt. Express* **16**, 12987–12994 (2008).

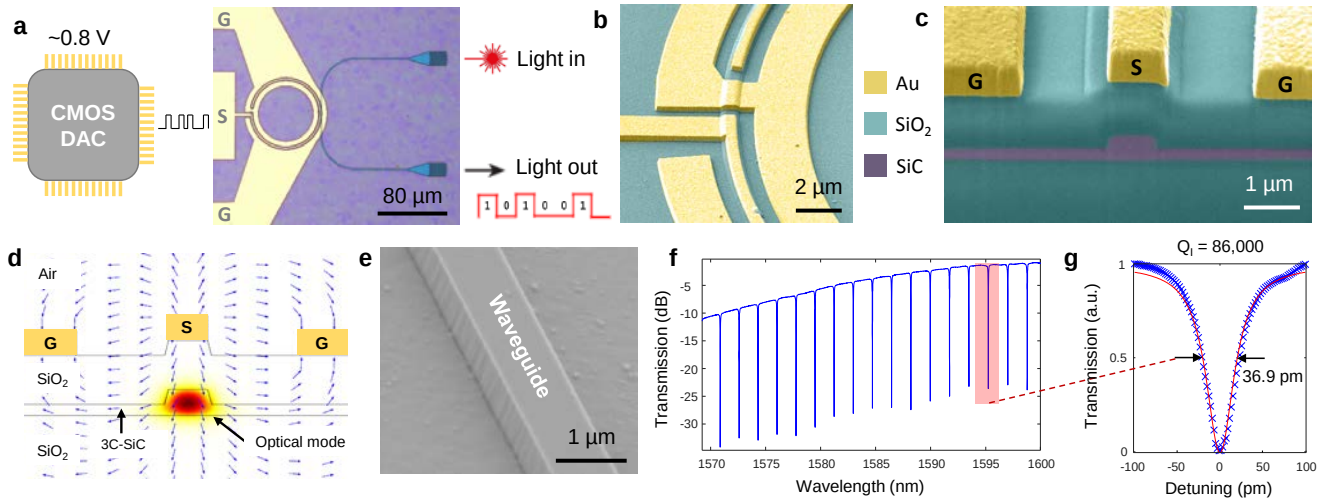

Fig. 1 Integrated Pockels modulator in SiC on insulator. (a) Overview of the fabricated ring modulator showing compatibility with CMOS voltages. (b) False color SEM of the microring waveguide and modulator electrodes. (c) False color SEM cross-section of the active region of the modulator. (d) Simulated static electric field and optical mode of the active region of the modulator. (e) SEM of an etched waveguide with the sidewall shown. (f) Measured optical spectrum of the microring resonator. (g) Lorentz fit of the resonance lineshape to determine the intrinsic optical quality (Q_I) factor. (Cross: Measurement; Solid line: Lorentz fitting)

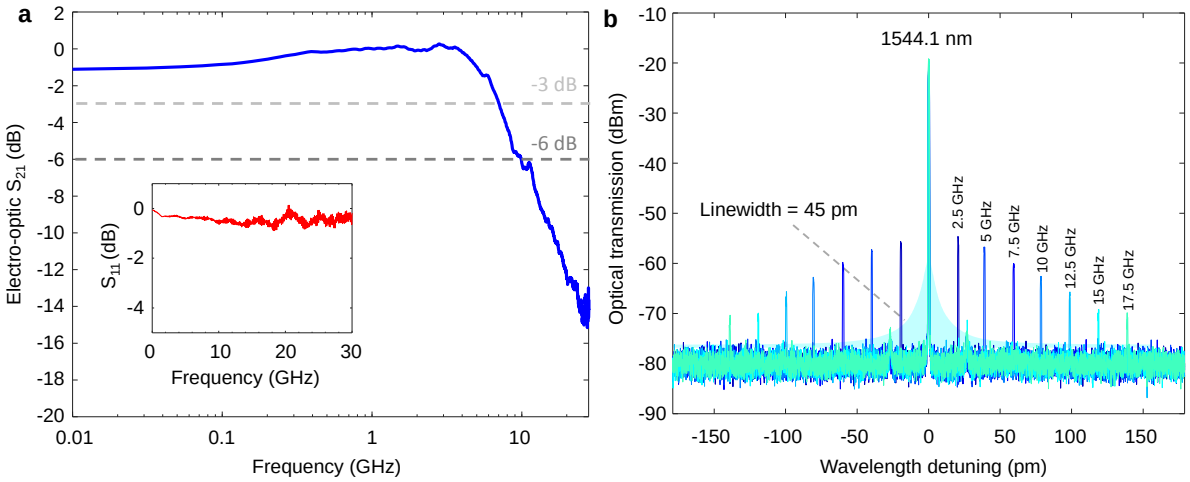

Fig. 2 Modulator bandwidth and EO characterization. (a) RF s-parameter characterization featuring a -3dB and -6dB bandwidths of 7.1 GHz and 9.9 GHz respectively. S_{21}, transmission coefficient of the scattering matrix. Inset shows the S_{11}, reflection spectrum of the modulator. (b) Optical spectrum at the output of the modulator for various input RF frequencies. The measurement at 2.5GHz which is within the resonator linewidth is used in the Pockels coefficient extraction.

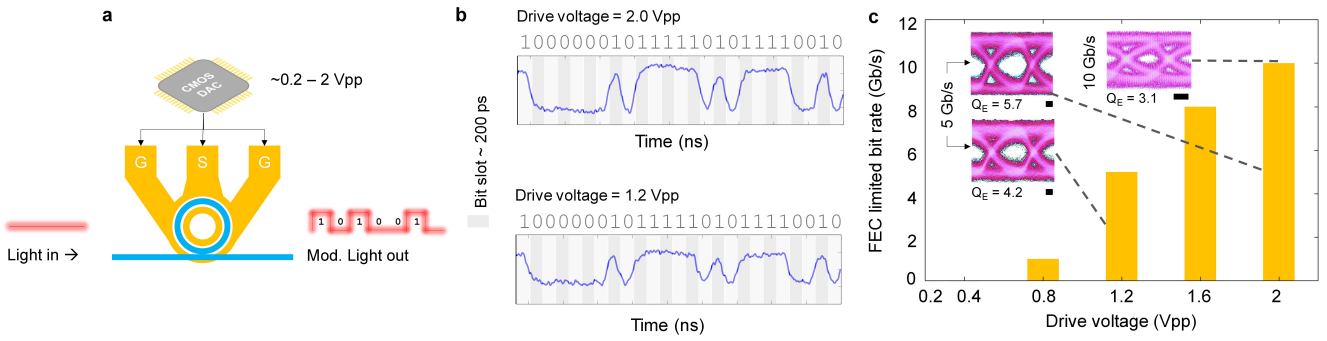

Fig 3. Digital CMOS level electro-optic modulation with NRZ PRBS of 2^7 bits. (a) Setup configuration using a CMOS DAC to drive the ground-signal-ground (GSG) electrodes of the modulator. (b) Time domain waveforms measured at the output of the modulator at 5 Gb/s for drive voltages of 2 Vpp and 1.2 Vpp respectively. (c) Drive-voltage-dependent eye-diagram quality (Q_E) factors for increasing bit rat. The Q_E factor greater than 2.7 corresponds to BER below the HD-FEC limit. Scale bars, 33 picoseconds.

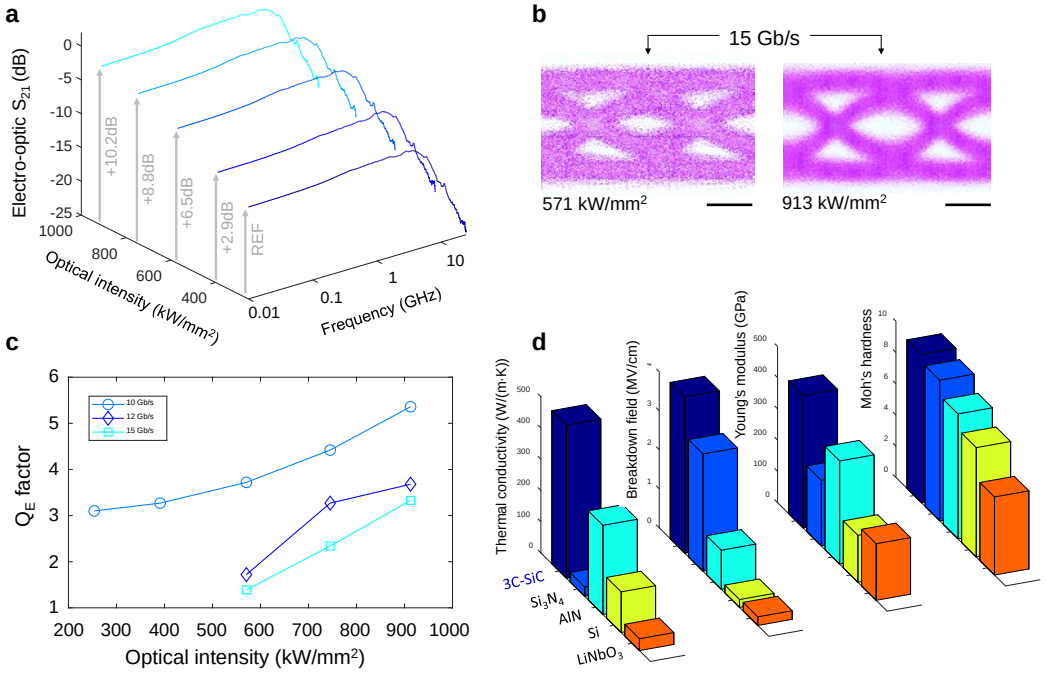

Fig 4. High power operation. (a) Electro-optic s-parameter characterization at high optical intensities showing an improvement in RF responses. (b) Measured eye diagrams at 15 Gb/s confirming the operation of the modulator at high optical intensities. (c) Q_E factors as a function of optical intensity for bit rates of 10 Gb/s, 12 Gb/s and 15 Gb/s showing an improved modulation performance for higher input intensity. (d) Material parameter comparison of 3C-SiC with widely used optical materials showing the distinct advantages of SiC for high power handling. Scale bars, 33 picoseconds.

Acknowledgements. We thank S. Desai for discussions on device simulation, and C. Yu for feedback on the manuscript. Device fabrication and characterization were carried out in part at the Harvard University Center for Nanoscale Systems (CNS), a member of the National Technology Coordinated Infrastructure Network, and the University of Sydney. This work was supported by Sydney Research Accelerator Fellowship and Harvard University Mobility Scheme. J. W. and D. M. acknowledge the support of Research Training Program Scholarships from the University of Sydney. N. S. acknowledges the support of the Natural Sciences and Engineering Research Council of Canada (NSERC), and NSF STC "Center for Integrated Quantum Materials" under Cooperative Agreement No. DMR-1231319. M. L. acknowledges support from Airforce Office of Scientific Research (AFOSR) under grant FA9550-19-1-0376.

Author contributions. K. P., M. L. and X. Y. conceived the experiment. K. P., L. L., A. S. and J. D. fabricated the devices. J. W. and D. M. performed numerical simulations. K. P., L. L., J. D. and N. S. carried out the device characterization. K. P., N.S. and X. Y. wrote the manuscript with contribution from all authors. M. L. and X. Y. supervised the project.

Competing interests. None.

Correspondence and requests for materials should be addressed to X. Y.

METHODS

Device fabrication. Devices are fabricated from a commercially available 3C-SiC on silicon wafer with 3.5 μm of SiC epitaxially grown on a silicon substrate supplied by NOVASiC. A 2 μm thick low pressure chemical vapor deposition (LPCVD) SiO_2 is deposited onto the SiC thin film, and the resultant stack is Van der Waals bonded to a thermal SiO_2 on silicon wafer before thinning down SiC via an inductive coupled plasma reactive ion etching (ICP-RIE) process. The device consists of a thin 3C-SiC layer, LPCVD SiO_2 and a silicon substrate for the handle. The waveguides and grating couplers are patterned on 2 μm of hydrogen silsesquioxane (FOX-16) resist using EBL. They are subsequently etched into the SiC layer using an ICP-RIE process consisting of the CMOS foundry compatible gases SF_6 and C_4F_8[26]. The built-up polymer due to C_4F_8 etch gas is removed using a two-step wet cleaning process. First, a solution of hydrogen peroxide and ammonium hydroxide is used to remove the polymer. Second, a solution of hydrogen peroxide and hydrochloric acid is used to remove the metal ions from the surface of the etched waveguides. Plasma enhanced chemical vapor deposition (PECVD) process is used to deposit a 1 μm layer of SiO_2 onto the fabricated devices to act as an insulation layer between the electrodes and the device, which is sufficiently thick to minimize excess absorption due to the metal electrodes. Device electrodes fabrication involves EBL patterning on Polymethyl methacrylate resist, developed with a mixed solution of 1 part Methyl isobutyl ketone and 3 parts Isopropyl alcohol. Metal layers consisting of 5 nm titanium and 500 nm of gold are deposited using electron beam evaporation followed by lift-off using a solution of N-Methyl-2-pyrrolidone.

Electro-optic characterization and transmission spectrum measurement. Laser light (Keysight 81960A) around 1550 nm is amplified using an erbium doped fiber amplifier (EDFA) followed by an optical bandpass filter to reduce amplified spontaneous emission (ASE) noise. The resultant light is launched into the ring modulator (Extended Data Fig. 1a). The laser is tuned to a wavelength that matches

the most linear edge of a resonance to ensure minimal distortion in the modulated signal. A second EDFA is placed after the modulator to compensate for optical loss before the optical to electrical conversion via a 20 GHz photodetector (Discovery). A high-speed microwave probe (GGB) is used to deliver the modulation signal to the input port of the transmission line. To measure the EO response, the sinusoidal signal with sweeping frequency from a signal generator of a vector network analyzer (VNA, Keysight N5234A) is used to drive the modulator via the microwave probe, while the photodetector output is connected with the VNA receiver. EO response is obtained from the s-parameter of the VNA, where RF cable losses are calibrated out of the measured frequency responses. To measure the high-speed data modulation, electrical PRBS signals of voltage varied from 0.2 Vpp to 2 Vpp are generated from a 65 GS/s arbitrary waveform generator (AWG, Keysight M8195A) and then connected with the microwave probe (Extended Data Fig. 1b). A real-time digital sampling oscilloscope with an analogue bandwidth of 110 GHz (Keysight UXR series) is used to capture the received signal from the photodetector. The oscilloscope acts as the receiver for the PRBS, where a second-order phase locked loop is used for clock recovery to generate an eye diagram of the received data. The eye Q_E factor was measured directly from the oscilloscope using persistence mode for a fixed number of waveforms.

By scanning the wavelength of the tunable laser and detecting the optical power (Keysight N7744A) at the optical output of the modulator, the transmission spectra for different DC voltages are obtained. DC bias voltages from -20V to +20V are applied on the modulator ground-signal-ground electrodes, and the results are shown in Extended Data Fig. 2.

Pockels coefficient extraction. Finite element method solver (COMSOL Multiphysics) is used to simulate the optical mode profile and the electric field distribution inside the SiC waveguide. The electro-optic overlap integral is numerically calculated to evaluate the interaction of optical and electric fields[43]. The modulation index is determined using the Jacobi-anger expansion method which is obtained from the optical power ratio of the modulated sideband and the optical carrier. The voltage induced effective

index change of the fundamental transverse electric mode is calculated from the measured resonance shift, and then the EO coefficient of the 3C-SiC waveguide at the operating wavelength is derived correspondingly[38,44].

Material parameter comparison. Extended Data Table 1 lists the comparison of common photonic integration materials with 3C-SiC, specifically parameters related to power handling of the modulator. The Young's modulus and Moh's hardness are useful parameters for a broad range of applications. Moreover, the refractive index and electrical permittivity are also listed. Low electrical permittivity combined with a higher refractive index are favorable for a larger modulation efficiency at a given EO coefficient.

Data availability. The data sets generated and/or analysed during the current study are available from the corresponding authors on reasonable request.

43. Rao, A. & Fathpour, S. Compact lithium niobate electrooptic modulators. *IEEE Journal of Selected Topics in Quantum Electronics* **24,** 1-14 (2017).
44. Tazawa, H. *et al.* Ring resonator-based electrooptic polymer traveling-wave modulator. *J. Light. Technol.* **24**, 3514-3519 (2006).
45. Bhatnagar, M. & Baliga, B. J. Comparison of 6H-SiC, 3C-SiC, and Si for power devices. *IEEE Trans. Electron Devices* **40**, 645–655 (1993).
46. Guarino, A., Poberaj, G., Rezzonico, D., Degl'Innocenti, R. & Günter, P. Electro-optically tunable microring resonators in lithium niobate. *Nat. Photonics* **1**, 407–410 (2007).
47. Zhu, S. & Lo, G.-Q. Aluminum nitride electro-optic phase shifter for backend integration on silicon. *Opt. Express* **24**, 12501–12506 (2016).
48. Gao, Y., Tao, L., Tsang, H. K. & Shu, C. Graphene-on-silicon nitride waveguide photodetector with interdigital contacts. *Appl. Phys. Lett.* **112**, 211107 (2018).

49. Lee, Y. S. *et al.* Hybrid Si-$LiNbO_3$ microring electro-optically tunable resonators for active photonic devices. *Opt. Lett.* **36**, 1119–1121 (2011).

50. Li, H. H. Refractive index of silicon and germanium and its wavelength and temperature derivatives. *J. Phys. Chem. Ref. Data* **9**, 561–658 (1980).

51. Arbabi, A. & Goddard, L. L. Measurements of the refractive indices and thermo-optic coefficients of Si_3N_4 and SiO_x using microring resonances. *Opt. Lett.* **38**, 3878–3881 (2013).

52. Goel, S., Luo, X., Reuben, R. L. & Rashid, W. Bin. Atomistic aspects of ductile responses of cubic silicon carbide during nanometric cutting. *Nanoscale Res. Lett.* **6**, 589 (2011).

53. Arizmendi, L. Photonic applications of lithium niobate crystals. *Physica Status Solidi (A) Applied Research* **201**, 253–283 (2004).

54. Yushkov, Y., Oks, E., Zolotukhin, D. & Tyunkov, A. Properties of Thermo-Conductive Ceramic-Based Coatings Deposited Using Fore-Vacuum Plasma-Cathode Electron Source. *7th International Congress on Energy Fluxes and Radiation Effects (EFRE)*, 844–847 (IEEE, 2020).

55. Wang, D., Wang, Z., Wang, Z., Qian, G. & Gong, X. Study on hydrocyclone separation enhancement of micro Si/SiC from silicon-sawing waste by selective comminution. *Sep. Sci. Technol.* 1–9 (2020).

56. Moskalewicz, T. *et al.* Electrophoretic deposition and microstructure development of Si3N4/polyetheretherketone coatings on titanium alloy. *Surf. Coatings Technol.* **350**, 633–647 (2018).

57. Weitzel, C. E. *et al.* Silicon carbide high-power devices. *IEEE Trans. Electron Devices* **43**, 1732–1741 (1996).

58. Stanicki, B. J. *et al.* Surface domain engineering in lithium niobate. *OSA Contin.* **3**, 345–358 (2020).

59. Lu, X., Moille, G., Rao, A., Westly, D. A. & Srinivasan, K. Efficient photoinduced second-harmonic generation in silicon nitride photonics. *Nat. Photonics* (2020).

60. Liu, X. *et al.* Highly efficient Thermo-optic Tunable Micro-ring Resonator based on thin film lithium niobate platform. *Opt. Lett.* **45**, 6318–6321 (2020).

61. Qiu, C. *et al.* All-optical control of light on a graphene-on-silicon nitride chip using thermo-optic effect. *Sci. Rep.* **7**, 1–7 (2017).

62. Wang, C., Zhang, M., Stern, B., Lipson, M. & Lončar, M. Nanophotonic lithium niobate electro-optic modulators. *Opt. Express* **26**, 1547–1555 (2018).

63. Watanabe, N., Kimoto, T. & Suda, J. The temperature dependence of the refractive indices of GaN and AlN from room temperature up to 515 °c. *J. Appl. Phys.* **104**, 106101 (2008).

64. Komma, J., Schwarz, C., Hofmann, G., Heinert, D. & Nawrodt, R. Thermo-optic coefficient of silicon at 1550 nm and cryogenic temperatures. *Appl. Phys. Lett.* **101**, 041905 (2012).

65. Jackson, K. M., Dunning, J., Zorman, C. A., Mehregany, M. & Sharpe, W. N. Mechanical properties of epitaxial 3C silicon carbide thin films. *J. Microelectromechanical Syst.* **14**, 664–672 (2005).

66. Jiang, W. C. & Lin, Q. Chip-scale cavity optomechanics in lithium niobate. *Sci. Rep.* **6**, 36920 (2016).

67. Xiong, C. *et al.* Aluminum nitride as a new material for chip-scale optomechanics and nonlinear optics. *New J. Phys.* **14**, 095014 (2012).

68. Han, S., Seok, T. J., Quack, N., Yoo, B. W. & Wu, M. C. Large-scale silicon photonic switches with movable directional couplers. *Optica* **2**, 370–375 (2015).

69. Xiong, W. *et al.* SiNx films and membranes for photonic and MEMS applications. *J. Mater. Sci. Mater. Electron.* **31**, 90–97 (2020).

Extended Data

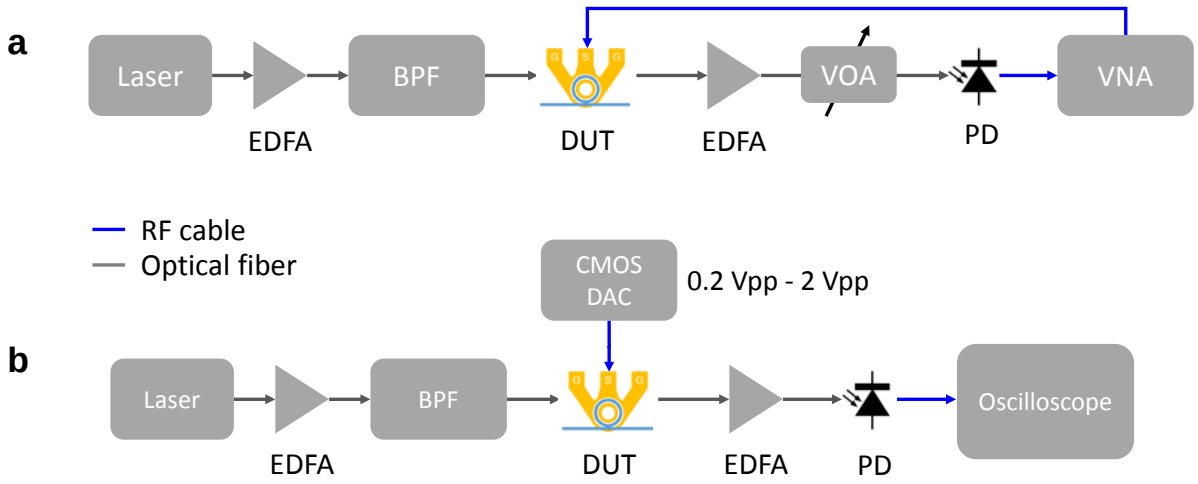

Extended Data Fig. 1 High speed measurement setups (a) Setup for measuring the EO response of the SiC modulator (b) Setup for testing the digital communications operation of the SiC modulator. EDFA, erbium doped amplifier; BPF, bandpass filter; DUT, device under test; VOA, variable optical attenuator; PD, photodiode; VNA, vector network analyzer.

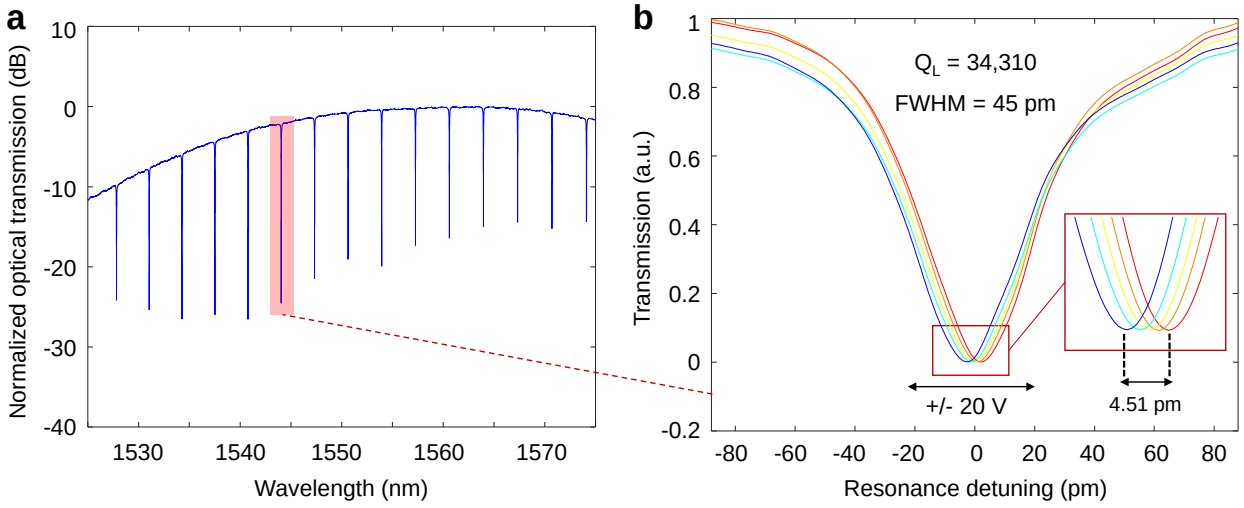

Extended Data Fig. 2. Optical characterization of the electro-optic ring modulator (a) optical transmission spectrum showing single mode operation (b) Measured DC electro-optic resonance detuning and the loaded quality (Q_L) factor of the modulator ring resonator over a DC voltage range of +/- 20 V. FWHM, full-width-half-maximum.

Extended Data Table 1 | Comparison of photonic integration platforms for power handling and robustness

	3C-SiC	$LiNbO_3$	AlN	Si	Si_3N_4
Relative permittivity	9.66 [45]	28 [46]	10 [47]	11.8 [45]	5.5 [48]
Refractive Index @ 1550 nm	2.57 [34]	n_o = 2.21 [49] n_e = 2.14	2.12 [9]	3.48 [50]	1.98 [51]
Moh's Hardness	9.5 [52]	5 [53]	8 [54]	7 [55]	9 [56]
Breakdown field	4 MV/cm [57]	220 kV/cm [58]	1 MV/cm [9]	200 kV/cm [45]	3 MV/cm [59]
Thermal conductivity	490 W/(m·K) [45]	38 W/(m·K) [60]	285 W/(m·K) [9]	130 W/(m·K) [9]	30 W/(m·K) [61]
Thermo-optic coefficient	5.8×10^{-5} K^{-1} [26]	3.9×10^{-5} K^{-1} [62]	2.3×10^{-5} K^{-1} [63]	1.8×10^{-4} K^{-1} [64]	2.5×10^{-5} K^{-1} [61]
Mechanical elastic/Young's modulus	424 GPa [65]	181 GPa [66]	330 GPa [67]	150 GPa [68]	210 GPa [69]